AIAA JOURNAL
Vol. 50, No. 10, October 2012

Study of a Compression-Ramp Interaction Using Large-Eddy Simulation/Reynolds-Averaged Navier–Stokes Models

Daniel A. Gieseking* and Jack R. Edwards†
North Carolina State University, Raleigh, North Carolina 27695

DOI: 10.2514/1.J051195

Two large-eddy simulation/Reynolds-averaged Navier–Stokes models are applied to a shock/boundary interaction generated by a 20 deg compression corner. The models are designed to transition from unsteady Reynolds-averaged Navier–Stokes to large-eddy simulation as the boundary layer shifts from its logarithmic behavior to its wakelike response, but they differ in that one model requires a preselection of a model constant for each problem, while the other computes this constant as a function of local and ensemble-averaged turbulence properties. Predictions are compared with mean-flow and second-moment experimental data obtained at Princeton University. In general, calculated mean-flow velocity, surface-pressure, and surface skin-friction distributions agree well with the experiment, with the most noticeable discrepancy being a slight overprediction of the level of upstream influence induced by the shock wave. Comparisons with mass-flux fluctuation intensity, Reynolds axial stress, and Reynolds shear-stress profiles are also presented. These show generally good agreement with experimental trends relating to Reynolds stress amplification and anisotropy modulation. The calculations also predict the existence of a low-frequency motion of the separation shock that is probably associated with the motion of the backflow region. Higher-frequency modulations of the shock front as induced by the passage of coherent, streaklike structures through the shock also appear to contribute to the measurable intermittency effects.

Nomenclature

c	=	local sound speed, m/s
C_f	=	skin friction
C_M	=	model constant for subgrid viscosity
C_N	=	new model constant for blending function
C_μ	=	turbulence model constant
d	=	distance to nearest wall, m
f_{sh}	=	shock-motion frequency, 1/s
k	=	turbulence kinetic energy, $(\text{m/s})^2$
L_{SM}	=	length over which separation shock translates, m
L_{sep}	=	length of separation region, m
M	=	Mach number
p	=	pressure, N/m^2
Pr_t	=	turbulent Prandtl number
q	=	flow property
R	=	gas constant, $\text{J/kg} \cdot \text{K}$
Re	=	Reynolds number
S	=	magnitude of vorticity vector, 1/s
S_L	=	shock-motion Strouhal number
T	=	temperature, K
u, v, w	=	velocities in x, y, z directions, m/s
u_j	=	velocity component in direction j, m/s
u_τ	=	friction velocity, m/s
t	=	time, s
t_{res}	=	flow-through time, s
x, y, z	=	distances in streamwise, wall-normal, spanwise directions, m
α	=	turbulence model constant
Γ	=	blending function
γ	=	intermittency function
δ	=	boundary-layer thickness, m
θ	=	structure angle, rad
ν	=	kinematic viscosity, m^2/s
ν_t	=	kinematic eddy viscosity, m^2/s
ξ	=	vorticity magnitude, 1/s
ρ	=	density, kg/m^3
τ	=	time scale, s
ϕ	=	turbulence model constant
ω	=	specific dissipation rate, 1/s

Subscripts

t	=	turbulent
w	=	wall
0	=	reference condition
∞	=	freestream

Superscripts

$'$	=	fluctuation
$+$	=	wall coordinates based on local kinematic viscosity and friction velocity

Presented as Paper 2011-0726 at the 49th AIAA Aerospace Sciences Meeting Including The New Horizons Forum and Aerospace Exposition, Orlando, FL, 4–7 January 2011; received 24 January 2011; revision received 4 January 2012; accepted for publication 12 February 2012.

*Graduate Research Assistant, Department of Mechanical and Aerospace Engineering. Student Member AIAA.

†Professor, Department of Mechanical and Aerospace Engineering. Associate Fellow AIAA.

I. Introduction

SHOCK-wave/turbulent boundary-layer interactions have been the subject of intensive study due to their importance in aerodynamics and propulsion of high-speed flight vehicles. Experimental efforts [1–11] have revealed many features of such interactions, including a large amplification of Reynolds stress components through the shock wave, significant changes in turbulence structure factors through the interaction, the presence of a dominant low-frequency signal associated with the motion of the separation shock, a transition to a wakelike velocity profile over the separation region, and a rapid recovery of the boundary layer to a new equilibrium state downstream of the reattachment location. The design and analysis of high-speed flight vehicles requires methods for predicting the aerodynamic loads, surface heat transfer, and boundary-layer displacement effects associated with such interactions.

Predictive capability of Reynolds-averaged Navier–Stokes (RANS) methods for shock-wave/turbulent boundary-layer interactions has been rather variable, with some features, such as the upstream influence induced by the shock wave, captured relatively well by certain models, but others, such as the recovery rate of the boundary layer downstream of the interaction, predicted poorly in general. Turbulence models, ranging from simple algebraic closures [12], to one- and two-equation models [13,14], to algebraic Reynolds stress [15] and full Reynolds stress closures, have been used [16], but the level of predictive capability does not necessarily increase with model complexity. Knight and Degrez [17] show that the RANS models tend to perform better for fundamentally three-dimensional interactions than they do for nominally two-dimensional (2-D) interactions, such as the flow over a compression-ramp or an oblique-shock impingement interaction. This probably indicates that such canonical flows have elements of three-dimensionality that are reflected in the experimental data but not necessarily in the calculations.

Higher-fidelity time-dependent models, such as direct numerical simulation (DNS), large-eddy simulation (LES), and hybrid LES/RANS models, represent a potential means of improving predictive capability for shock/boundary-layer interactions and for investigating fundamental aspects of their flow physics. Wu and Martin [18] have conducted a DNS of a compression-corner interaction and have obtained reasonable agreement with experimental data. Subsequent analyses [19] have used this database to examine correlations between the shock motion and upstream boundary-layer characteristics. Other DNS studies [20] have provided insights into the underlying mechanisms of shock oscillation in impinging-shock interactions but have not reported direct comparisons with experimental data. Wall-resolved LESs have been conducted for impinging-shock interactions [21,22]. Direct comparisons with experimental data have been made in these cases, but such comparisons are complicated by the fact that impinging-shock interactions in wind tunnels invariably produce a three-dimensional separation pattern that cannot be reproduced correctly in calculations that assume statistical two-dimensionality. The LES simulations of Touber and Sandham [22] are of particular interest, as they performed the simulations for a period of time long enough to delineate precisely the broadband characteristics of low-frequency separation-shock motion. Compression-corner interactions appear less sensitive to wind-tunnel effects, and reasonably accurate LES simulations of a compression-corner flowfield have been obtained by Loginov et al. [23]. Wall-resolved LES simulations are restricted to a low or moderate Reynolds number due to the need to capture structural changes in near-wall turbulence. Hybrid LES/RANS techniques [24–28], in contrast, seek to model the effects of near-wall turbulence through unsteady RANS concepts. While many challenges still remain in merging the closure strategies, the fact that such techniques are not restricted according to Reynolds number makes them attractive alternatives to LES or DNS for examining the general structure of shock/boundary-layer interactions. Considering that most of the more detailed experimental databases are at Reynolds numbers too large for an affordable wall-resolved LES, LES/RANS methods are the only current alternative for high-fidelity time-dependent simulations of these experiments.

This paper focuses on the continued evaluation of a new LES/RANS model [26] for shock-wave/boundary-layer interactions. The model uses a combination of ensemble-averaged and local data to target the instantaneous RANS-to-LES transition where an attached boundary layer shifts from its logarithmic structure to its wakelike response. Results reported in [26] show that the new model provides accurate mean and second-moment statistics for an array of flat-plate boundary layers at different Reynolds numbers as well as for nominal Mach 3 flow over a 16 deg smoothly turning compression corner [8]. In this paper, we evaluate the model's performance for another experiment performed at Princeton University: nominal Mach 3 flow over a 20 deg compression corner [4–7]. A wealth of experimental data is available for this case, including mean-flow measurements (deduced from pitot surveys) throughout the interaction region, Reynolds stress measurements deduced from constant-temperature hot-wire anemometry, surface-pressure and skin-friction distributions, and surface oil-flow images. This case exhibits axial separation, and aspects of the motion of the separation shock have been analyzed by Dolling and Or [10]. The outline of this paper is as follows. In Sec. II, the LES/RANS models and numerical methods employed are described in brief. Section III presents details of the mesh, boundary conditions, and time-advancement procedure. The results of this investigation, emphasizing comparisons with experimental data and analyses of time-dependent features of the interaction, are presented in Sec. IV. Finally, some concluding remarks are presented in Sec. V.

II. Large-Eddy Simulation/Reynolds-Averaged Navier–Stokes Models and Numerical Methods

A. Large-Eddy Simulation/Reynolds-Averaged Navier–Stokes Models

Two LES/RANS models are considered in this work. For each, the Menter baseline (BSL) model [29] is used as the basis, and the modification only involves the alteration of the eddy viscosity field according to the following prescription:

$$\nu_t = \Gamma \nu_{t,\mathrm{RANS}} + (1-\Gamma)\nu_{t,\mathrm{LES}} \tag{1}$$

where $\nu_{t,\mathrm{RANS}} = \frac{k}{\omega}$ is obtained from the Menter BSL model, and the subgrid eddy viscosity is defined as

$$\nu_{t,\mathrm{LES}} = \Gamma \kappa C_\mu^{1/4} k^{1/2} d + (1-\Gamma)\bar{\nu}_{t,\mathrm{LES}} \tag{2}$$

with

$$\bar{\nu}_{t,\mathrm{LES}} = C_M S^{1/2}(q^2)^{1/4}\Delta^{3/2}, \qquad C_M = 0.06$$
$$q^2 = \tfrac{1}{2}(\tilde{u}_k - \hat{\tilde{u}}_k)^2 \tag{3}$$

from Lenormand et al. [30]. The additional blending implied in Eq. (2) serves to equate the subgrid-scale eddy viscosity with the log-law value $\nu_{t,\log} = \kappa u_\tau d$ where the unsteady RANS component of the model is active. The filter width Δ is taken to be the cube root of the cell volume, and S is the magnitude of the vorticity vector.

A flow-dependent blending function Γ is used to shift the model from unsteady RANS to LES. In the first model, reported in [24,25],

$$\Gamma = \frac{1}{2}\left(1 - \tanh\left[5\left(\frac{1}{\lambda_C^2} - 1\right) + \phi\right]\right), \qquad \phi = \tanh^{-1}(0.98) \tag{4}$$

$$\lambda_C = \alpha_1 \frac{\sqrt{v}}{C_\mu^{1/4}\sqrt{\kappa} d \sqrt{\omega}} \tag{5}$$

with the model constant α_1 fitted for the experimental conditions and geometry of [5] as $\alpha_1 = 13.057X + 76.703$, where X is the surface distance in meters with the origin at the apex of the compression corner. As discussed in [25], this fitting procedure is designed to ensure that the time-averaged transition from RANS to LES takes place approximately at the location where the inflow boundary layer shifts from its logarithmic structure to its wakelike structure.

A newer model, developed in [26], is also considered in this work. This model does not require a case-by-case prescription of a model constant. The blending function for this model is defined as

$$\Gamma = \frac{1}{2}\left(1 - \tanh\left[15\left(\frac{1}{\lambda_N^2} - 1\right)\right]\right) \tag{6}$$

$$\lambda_N = C_N \sqrt{10 + \frac{\bar{k} + \bar{k}_R}{v\bar{\omega}}} \frac{\sqrt{v}}{C_\mu^{1/4}\kappa d \sqrt{\omega}} \tag{7}$$

In this expression, $\bar{k}$ is the ensemble-averaged modeled turbulence kinetic energy, $\bar{k}_R$ is the ensemble-averaged resolved turbulence kinetic energy,

$$\bar{\rho}\bar{k}_R = \frac{1}{2}\left(\overline{\rho u_k u_k} - \frac{\overline{\rho u}_k \overline{\rho u}_k}{\bar{\rho}}\right) \tag{8}$$

and ω and $\bar{\omega}$ are instantaneous and ensemble-averaged modeled specific dissipation rates, respectively. The combination of instantaneous and ensemble-averaged data allows the RANS-to-LES transition position $\Gamma = \frac{1}{2}$ to fluctuate dynamically about a mean value that is a function of the local ensemble-averaged state of the flow. The model constant $C_N \sim 1.5$ was determined by comparing results from this model with those of the original for several canonical flows. As it is dependent on both inner-layer and outer-layer length scale information, this model should more capable of adjusting to departures from local equilibrium, and no problem-specific calibration is required. The required ensemble averages are currently computed using an exponentially weighted moving average: $\bar{Q}^n = \bar{Q}^{n-1}(1 - A) + AQ^n$, with $A = \frac{\Delta t}{\tau}$. The time scale τ is defined as follows for two variants considered in this work:

$$\text{Weighting 1: } \tau = t$$

$$\text{Weighting 2: } \tau = \min(t, t_{\text{res}}), \qquad t < 4t_{\text{res}}$$

$$t - 3t_{\text{res}}, \qquad t \geq 4t_{\text{res}}$$

$$t_{\text{res}} = \frac{L}{U_\infty} \tag{9}$$

where L is the length of the domain (0.5 m), and U_∞ is the freestream velocity. Weighting method 2 assumes that a statistically stationary state should emerge after four flow-through times (t_{res}): after that point, a conventional time average is calculated.

B. Numerical Methods

The LES/RANS models are implemented into a finite volume Navier–Stokes solver written for general gas mixtures. The Boussinesq hypothesis is used to relate the modeled Reynolds stress to the rate of strain, and Fourier's law, parameterized by constant values of the laminar and turbulent Prandtl number (0.72 and 0.9, respectively), is used to model the heat flux vector. A recycling–rescaling technique [25] applied to the fluctuation fields is used to sustain large-eddy motion. A random-walk procedure is used to shift the recycled fluctuation field in the spanwise direction to reduce the possibility of artificial three-dimensional features in the time-averaged incoming boundary layer. Discrete times at which shifting occurs and the distance of the shift are determined by sampling Gaussian distributions of a time scale associated with a specified streak length and a specified fraction of the boundary-layer thickness. These discrete times and distances are connected by straight lines to form a continuous shifting pattern. More details of this procedure can be found in [31]. A second-order Crank–Nicholson scheme is used for time advancement. The basic first-order upwind method is extended to higher order using a low-dissipation scheme (termed LD-PPM) formed by blending the piecewise-parabolic method (PPM, [32]) with a fourth-order central scheme according to a flow-dependent switch developed by Ducros et al. [33].

III. Calculation Details

Freestream conditions for this calculation are shown in Table 1. The mesh used in the calculations extends from $X = -0.35$ m to $X = 0.175$ m (21 δ_0, $\delta_0 = 2.5$ cm), with $X = 0$ being the apex of the 20 deg wedge. Mesh lines are generally orthogonal to the surface except in the vicinity of the corner. The mesh extends 0.125 m (5 δ_0) in the surface normal direction (Y) and from $Z = -.075$ m to $Z = 0.075$ m (6 δ_0) in the spanwise direction. The mesh spacing is such that 20 cells/δ_0 are present in the axial (X) and transverse (Z) directions in the upstream boundary layer. The X spacing decreases near the corner to a level of 45 cells/δ_0 before expanding again to the 20 cells/δ_0 value at the end of the domain. Significantly more cells are present within the boundary layer in the surface normal direction, and the minimum spacing near the wall is 5×10^{-6} m, which corresponds to a minimum Y^+ of 0.99 in the incoming boundary layer. The total number of interior mesh cells is $536 \times 200 \times 120 =$ 12.864 million cells. The recycle plane is located 8 δ_0 downstream of the inflow plane. Periodic boundary conditions are imposed in the spanwise direction, extrapolation conditions are applied at the outflow boundaries ($X = 0.175$ m, $Y = 0.125$ m), and no-slip boundary conditions are applied at the wall. The wall temperature is fixed at 1.03 T_0, where T_0, is the freestream stagnation temperature. The recycling/rescaling methods described in the previous section are used to sustain turbulence at the inflow plane ($X = -0.35$ m).

Table 1 Freestream and boundary-layer properties

Parameter	Value
Case	Smits and Muck [5]
M_∞	2.79
δ_0, mm	25
U_∞, m/s	562
Re_δ	1.58×10^6
P_o, Pa	6.9×10^5
T_o, K	263
Cf	1.07e − 3

To initialize the calculation, a 2-D RANS simulation of the incoming boundary layer was performed, followed by a 2-D RANS simulation of the interaction itself, both using the Menter BSL model. Re-scaled turbulent fluctuations obtained from an earlier calculation were superimposed onto the flat-plate boundary-layer solution, and the LES/RANS solution was initiated from this point. The LES/RANS solutions were evolved for a period of 0.0033 s ($\sim$75 $\delta_0/U_\infty = 3.57$ domain residence times) to remove initial transients. Statistics were then collected for an additional 0.0067 s ($\sim$150 $\delta_0/U_\infty = 7.14$ domain residence times). One case ($C_N =$ 1.5, weighting 1) was evolved an additional 0.01 s ($\sim$230 δ_0/U_∞) to collect data at X-Z planes located at the surface, at $Y/\delta_0 = 0.2$, and at $Y/\delta_0 = 0.7$ for purposes of temporal analysis and animation of the flowfield response.

IV. Results

A. Mean-Flow Properties

Figure 1 shows instantaneous and averaged views of the temperature at the centerplane of the computational domain. The shear layer shifts from a boundary-layer structure to a wakelike structure as it moves over the separation region. A separation shock is formed at the upstream edge of a small region of flow separation located upstream of the corner. This shock induces some initial compression of the boundary layer, but the majority of the compression occurs through a sequence of Prandtl–Meyer waves that eventually coalesce outside the boundary layer to form a shock wave. Predictions of axial velocity and mass-flux fluctuation intensity in the inflow boundary layer are presented in Fig. 2a. Good agreement with the measured velocity profile is indicated, although the $C_N = 1.2$ case does show an overestimation of the velocity in the near-wall (logarithmic) region. This is associated with a thinner RANS-modeled region and an accumulation of resolved turbulence energy near the wall. The mass-flux fluctuation intensity profiles are in good agreement with experimental data away from the wall but consistently are higher close to the wall ($Y/\delta_0 < 0.4$). Resolved Reynolds axial and shear stresses in the inflow boundary layer are shown in Fig. 2b. The rapid drop in the stress levels for $Y/\delta_0 < \sim 0.2$ is due to the RANS component of the closure. The Choi et al. model [25] has the largest RANS region and reduces the resolved fluctuation content more than the others.

Computed pressure distributions are compared with experimental data in Fig. 3. While all models capture the shape of the experimental distribution to good accord, all overpredict the level of upstream influence, as quantified by the location of the initial pressure rise. Skin-friction distributions in Fig. 4 again indicate that all models

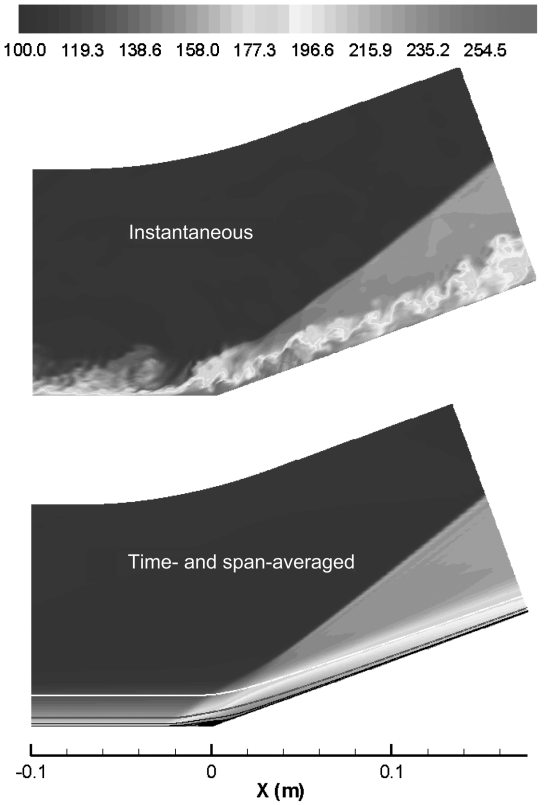

Fig. 1 Instantaneous and averaged temperature contours (K) near interaction region (streamline passes through $Y/\delta = 0.2$; white streamline passes through $Y//\delta = 0.7$).

capture a larger region of reversed flow, with the new models showing some improvement in this regard. The reattachment position is slightly overestimated by all models, and the skin-friction level in the recovery region is also overpredicted. The LES/RANS model with $C_N = 1.2$ yields upstream skin-friction levels 10% less than observed in the experiment and in the predictions of the other models. Overall, the pressure and skin-friction results indicate that the computed shock/boundary-layer interaction is stronger than observed in the experiment. This fact affects the interpretation of the entire structure of the flow, as the boundary layer responds, in general, to the displacement effect and dynamics induced by the region of low-momentum (sometimes) separated flow near the corner. Figure 5 shows that the effects of a larger low-momentum region are to induce a larger wake deficit in the velocity profiles near the corner. The $C_N = 1.2$ predictions are slightly better in this regard, as the overall extent of the separation region is smaller. This trend appears to be due to the accumulation of resolved turbulence energy mentioned earlier for this choice of the model constant, which leads to a fuller velocity profile in the logarithmic region (but not near the wall). The recovery of the boundary layer toward a new equilibrium state proceeds more slowly in the calculations than in the experiment, an effect that is again a consequence of a larger predicted region of low-momentum flow.

Indications of the effects of mean three-dimensionality are shown in Fig. 6, a plot of streamlines and skin-friction values at the X-Z surface plane. The contour range is from 0.0009 to 0.0011 to clearly indicate regions of very low-momentum fluid. Lines of coalescence on the ramp surface indicate the presence of pairs of longitudinally oriented counter-rotating vortex pairs embedded within the mean boundary layer. The lines of coalescence are associated with lower skin-friction levels and are separation lines in the sense that near-wall fluid is being lifted away from the surface through the actions of the vortices. The vortices themselves originate as the external boundary-layer flow spills around isolated low-momentum pockets of fluid that protrude onto the ramp surface. These, in turn, originate from inhomogeneities in the incoming boundary layer. The spanwise spacing of the vortex pairs is $\sim 2\ \delta_0$, which is consistent with prior numerical [23,24] and experimental work (reported in [23]). Loginov et al. [23] argue that the growth of these structures may result from a Görtler instability mechanism, given the degree of streamline curvature present as the boundary layer separates, then reattaches on the wedge surface. The pattern shown in the predictions of Fig. 6 is not universal: different models and initial conditions will lead to different placements of the vortical structures, but the spacing between the units remains approximately constant.

B. Reynolds Stress Profiles

Figures 7–9 present mass-flux fluctuation intensity, Reynolds axial stress, and Reynolds shear-stress distributions at different streamwise stations. The Reynolds stress tensor expressed in Cartesian coordinates is rotated to align with the surface for $X < -0.0302$ and $X > 0.0181$. For $-0.0302 < X < 0.0181$, the rotation angle is selected to be 5.5 deg, per the experiment [5]. The evolution of the mass-flux fluctuation intensity (Fig. 7), computed as

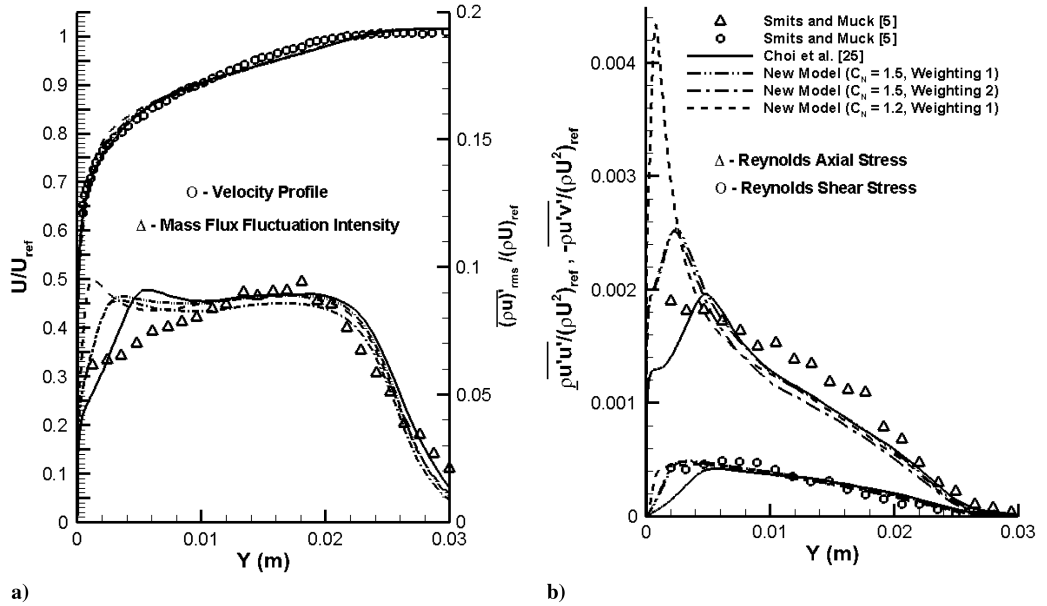

Fig. 2 Inflow boundary-layer mean and fluctuating properties: a) mean velocity and mass-flux fluctuation intensity; and b) Reynolds axial and shear stress.

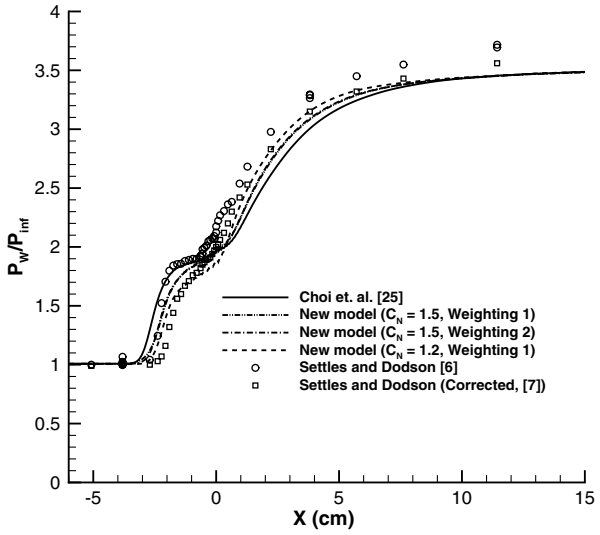

Fig. 3 Surface-pressure distributions.

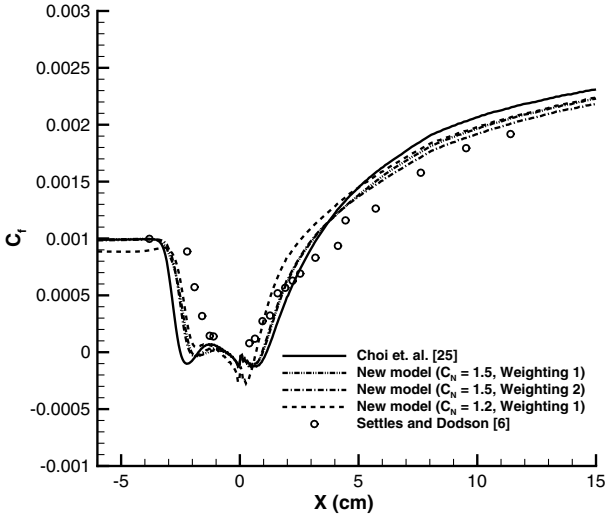

Fig. 4 Surface skin-friction distributions.

$$([\overline{(\rho u_1)'}]^2)^{1/2} = [\overline{(\rho u_1)^2} - \overline{\rho u_1}\,\overline{\rho u_1}]^{1/2} \tag{10}$$

is generally in close agreement with the experimental trends once the boundary layer begins to recover (stations downstream of $X = 0.0414$ m). Within the separation region ($X = -0.0063$ to $X = 0.0127$ m), the computations generally underpredict the peak

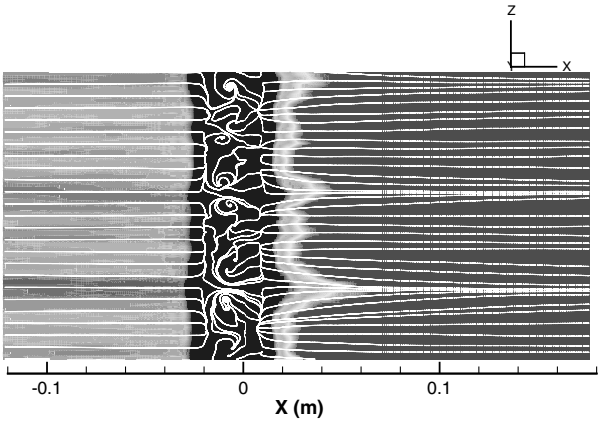

Fig. 6 Surface skin-friction contours (scaled from 0.0009 to 0.0011).

fluctuation intensity. The location of the perturbation in the fluctuation intensity due to the shock wave is more sensitive to the LES/RANS model variant and correlates with the relative effects of each model in predicting the level of upstream influence. Resolved-scale Reynolds axial and shear-stress distributions, computed using Favre averages according to

$$\bar{\rho}\,\overline{u_i' u_j'} = \overline{\rho u_i u_j} - \frac{\overline{\rho u_i}\,\overline{\rho u_j}}{\bar{\rho}} \tag{11}$$

are plotted in Figs. 8 and 9. Only profiles upstream of the interaction and downstream of the reattachment location are shown in these figures; the general trends for locations within the separation region are similar to those evidenced at the $X = 0.0254$ m station. Far downstream, agreement with experiment for the Reynolds axial stress (Fig. 8) is excellent, but in near-wall regions just downstream of the reattachment point, the computations overpredict the experiment by more than a factor of 2. Also shown are predictions extracted using Morkovin's strong Reynolds analogy (SRA) [34,35] as implemented by Smits and Muck [5]:

$$\bar{\rho}\,\overline{u_1' u_1'} = \frac{1}{\beta^2}\frac{\overline{[(\rho u_1)']^2}}{\bar{\rho}} \tag{12}$$

Here, $\beta^2 = 1 - 2R_{uT}(\gamma - 1)M_1^2 + [(\gamma - 1)M_1^2]^2$ [2], with M_1 being the local average Mach number evaluated as u_1/c, where c is the local sound speed, and R_{uT} is the correlation coefficient

$$\overline{u_1' T'}\Big/\left(\overline{(u_1')^2}\right)^{1/2}\left(\overline{(T')^2}\right)^{1/2}$$

In Smits and Muck [5], the correlation coefficient R_{uT} is set equal to -0.8 [36], whereas Morkovin's SRA [34] assumes R_{uT} equal to

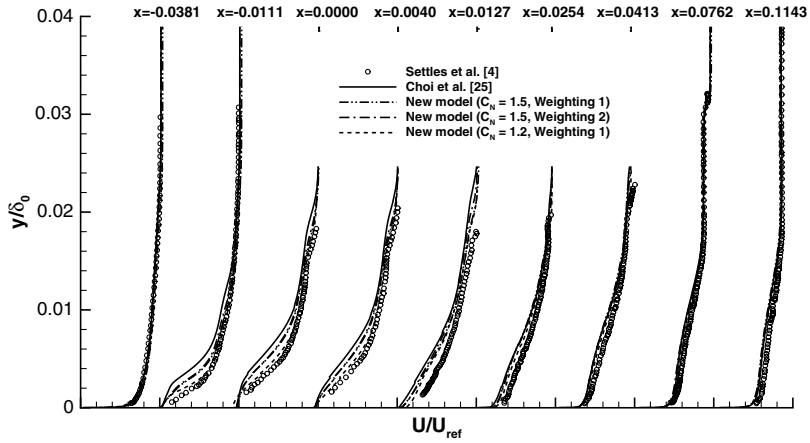

Fig. 5 Velocity profiles throughout the interaction region.

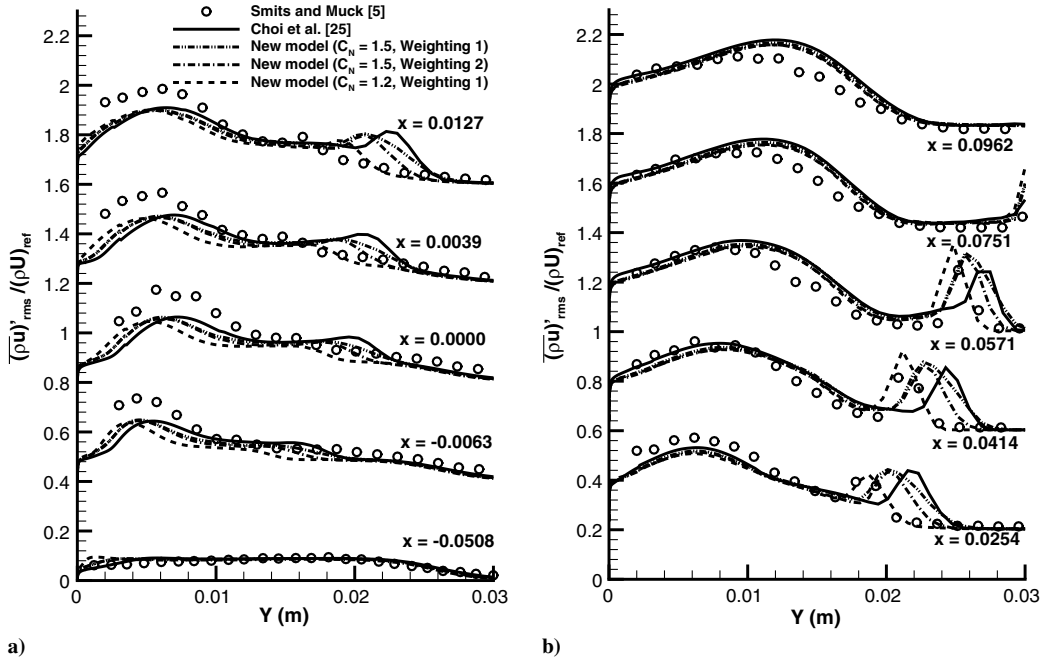

Fig. 7 Mass-flux fluctuation intensity distributions.

−1.0. The SRA predictions correspond to one specific model variant ($C_N = 1.2$, weighting method 2). The use of the SRA yields slightly larger estimates of the Reynolds axial stress, but overall, the differences are very minor and do not explain the observed discrepancies in the near-wall region. Considering that the numerical methods actually underpredict the peak fluctuation intensity for these profiles, the origin of the discrepancy must relate to the structure of the mean flow, specifically to the fact that the LES/RANS techniques predict a larger low-momentum region, which leads to lower mean density values and lower values for β^2.

Resolved Reynolds shear-stress distributions are plotted in Fig. 9. At all stations excepting the upstream one, the calculations significantly overpredict the measured levels. The predicted Reynolds shear-stress amplification trends are in accord with those exhibited for the Reynolds axial stresses and the fluctuation intensities. The experimental measurements indicate that the Reynolds shear stress responds much more slowly to the interaction. Using the SRA, the Reynolds shear stress is calculated as $\bar{\rho}\,\overline{u_1' u_2'} = \frac{1}{\beta}\overline{(\rho u_1)' u_2'}$. Predictions using the SRA are closer to the experiment. It should be noted that experimental uncertainties for the Reynolds shear-stress measurements are estimated as being from −32 to +12% in the upstream boundary layer. No error estimates are given for the interaction or recovery regions, but it is argued [2,5] that calibration difficulties might limit the utility of the inclined-wire measurements for mean Mach numbers (resolved normal to the wire) less than 1.2. It should also be noted that Kuntz et al.'s study [37] of a similar compression-ramp interaction using laser Doppler velocimetry yielded Reynolds shear-stress values downstream of the

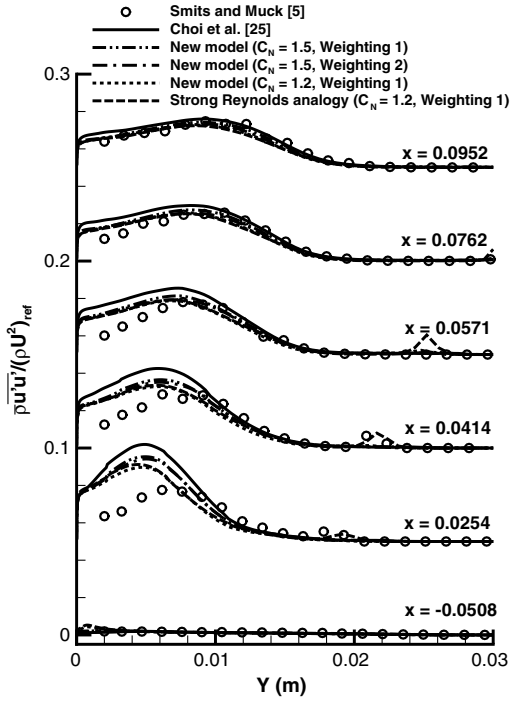

Fig. 8 Reynolds axial stress distributions.

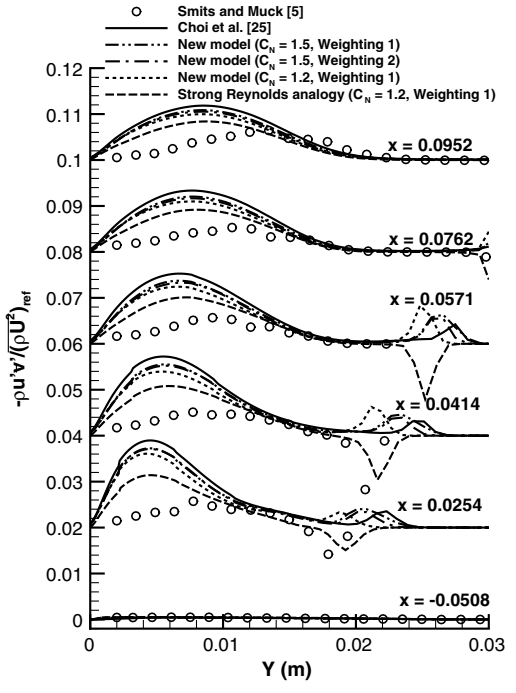

Fig. 9 Reynolds shear-stress distributions.

interaction that were more than twice as large as Smits and Muck's [5] measurements.

C. Reynolds Stress Evolution Along Streamlines

Figure 10 shows the evolution of the Reynolds stress tensor along streamlines originating at $X = -10$ cm, $Y/\delta_0 = 0.2$, 0.4, and 0.6. The Reynolds stresses are extracted using Favre-averaging [Eq. (10)] and are expressed in a coordinate system rotated to follow the streamline path. As in [5], the stress components are normalized by $\overline{u_1' u_1'}$ in the upstream boundary layer. The separation shock causes some amplification of the Reynolds stress components, but the majority of the amplification takes place as the flow compresses further downstream. Additional amplification may occur through shear-layer instability growth mechanisms [22,38,39]. The peak Reynolds stress values occur near the surface just downstream of the reattachment point. Disturbances in the Reynolds stresses originating at this location diffuse and advect outward and downstream. The peaks observed for streamlines originating from positions further outward in the upstream boundary layer are more of a consequence of the streamlines intersecting this disturbance field than of an amplification effect occurring directly along the streamlines. Comparisons with experimental data from [5] indicate that, as expected, the LES/RANS model used ($C_N = 1.2$, weighting 1) overestimates the amplification effect near the wall ($Y/\delta_0 = 0.2$). Agreement is better for streamlines originating further out into the boundary layer. Peak amplification factors in the range of 8 to 13 are observed, relaxing back to a range of 3 to 6 at $X = 15$ cm. In general, the amplification factors for $\overline{u_1' u_1'}$ and $\overline{u_1' u_2'}$ are similar and are the highest, followed by those of $\overline{u_2' u_2'}$ and $\overline{u_3' u_3'}$.

D. Reynolds Stress Anisotropy

The structure factors $\overline{u_1' u_1'}/2k$, $\overline{u_2' u_2'}/2k$, $\overline{u_3' u_3'}/2k$, and $\overline{u_1' u_2'}/2k$ are plotted in Fig. 11 for the same streamlines as used above. It is clear that the passage of the flow through the separation shock induces a transfer of fluctuation energy from the axial component $\overline{u_1' u_1'}$ to the normal and lateral components $\overline{u_2' u_2'}$ and $\overline{u_3' u_3'}$. This redistribution is reasonably modeled by the rapid distortion approximation (RDA) analysis of Debieve et al. [40] as applied by Smits and Muck [5], although the absolute changes in the structure factors predicted through RDA are everywhere larger than shown in the calculations. However, the RDA appears only to hold just past the separation shock: further downstream, a reversal of the energy-transfer process occurs, peaking at approximately the reattachment position. Here, fluctuation energy is transferred from the transverse and lateral components to the axial component. Downstream of the reattachment location, the structure factors begin to relax back to a new equilibrium state, but it is clear that the axial extent of the domain is too short for a complete recovery of the boundary layer. The structure factor $\overline{u_1' u_2'}/2k$ also increases from its upstream value of $\sim$0.16 to peak values in a range of 0.27 to 0.32 at the shock position before relaxing back to values similar to those in the incoming boundary layer. The constancy of such structure factors along a streamline is an important assumption in algebraic Reynolds stress models, and it is clear that the separation/reattachment process induces complex behavior that would invalidate this assumption. Menter's shear-stress transport (SST) turbulence model [29], which can be viewed as a simplified form of an algebraic Reynolds stress technique, shifts its Reynolds stress closure in regions of high strain rate to

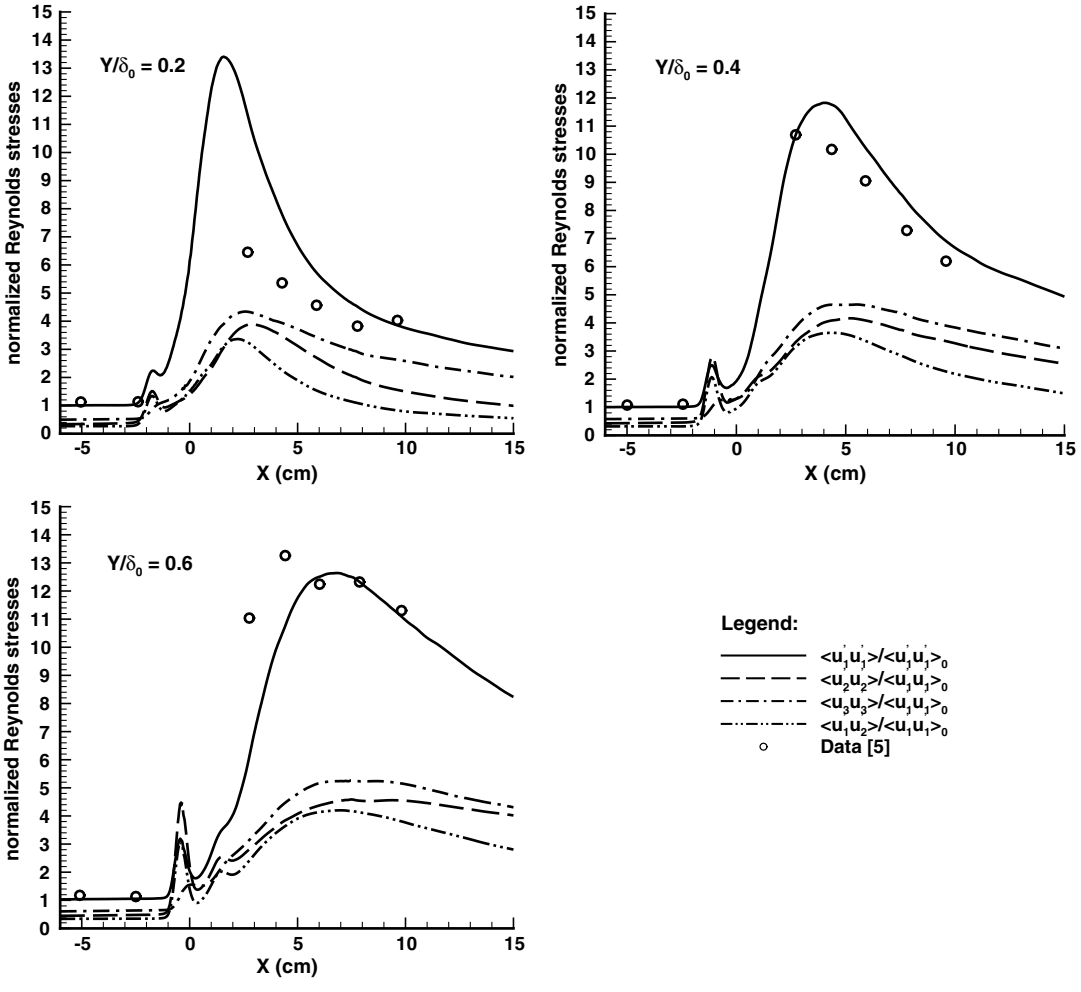

Fig. 10 Reynolds stress amplification along streamlines.

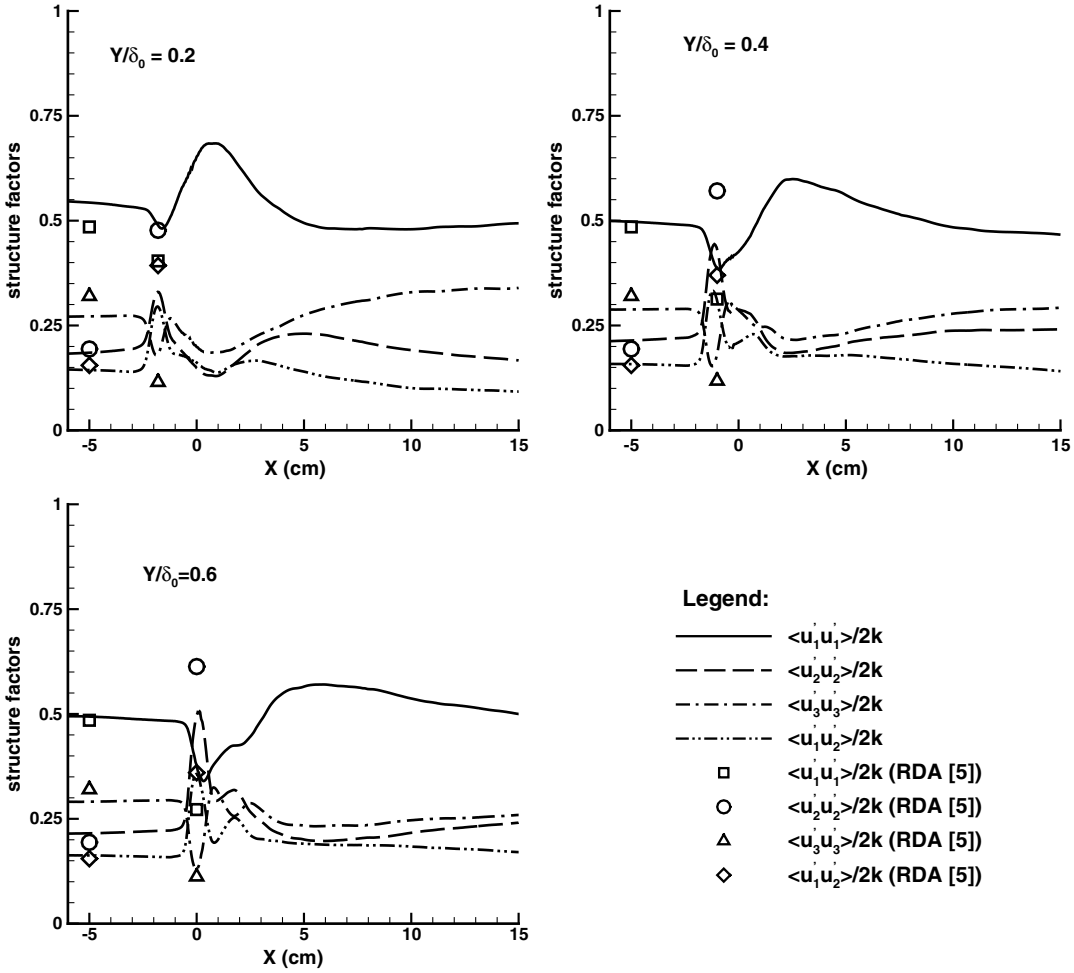

Fig. 11 Structure-factor evolution along streamlines.

$$-\overline{u_i' u_j'} = \frac{2a_1 k}{S}\left(S_{ij} - \frac{1}{3}\delta_{ij}S_{kk}\right) - \frac{2}{3}\delta_{ij}k \tag{13}$$

where S is the vorticity magnitude and S_{ij} is the strain rate tensor. The structure factor a_1 used in this relation is $\overline{u_1' u_2'}/k = 0.3$, which is close to that predicted above in the upstream boundary layer but half of that calculated in the vicinity of the shock front. This may explain why, for this interaction, Menter's SST model produces a separation length approximately twice of that observed in the experiment and in the LES/RANS calculations.

E. Shock Motion

Separation-shock motion as induced both by the passage of organized turbulent structures through the shock and by a lower-frequency bulk motion of the separation region plays an important role in the dynamics of a compression-corner interaction [9–11]. The length L_{SM} over which the separation shock moves can be quantified by an intermittency (γ), defined as the fraction of time that the separation shock is ahead of a particular X location. Figure 12 shows this distribution compared with the data of Dolling and Or [10]. The boundary-layer thickness in the Dolling–Or experiment is slightly smaller that in the Smits and Muck [5] experiment ($\delta_0 = 2.2$ cm versus 2.5 cm), and as such, the Dolling and Or data [10] are rescaled to conform to the thicker boundary layer. Even with this rescaling, the predicted intermittency distribution lies upstream of the experimental one, again indicative of the fact that the LES/RANS models capture a larger separation region. The shape of the intermittency distribution is in good accord with the experimental data, and the deduced L_{SM} is 0.6 δ_0 as compared with 0.7 δ_0 from [10]. This estimate is obtained by determining the X distance between the $\gamma = 0.04$ and $\gamma = 0.98$ stations. The probability of reversed axial flow near the surface is also shown in Fig. 12. A value of 1 at a particular location means that, for the entire sample time, the axial velocity just away from the surface is negative. There is no station for which flow reversal is maintained at all times. The flow is most likely to be reversed just downstream of the corner, and even further downstream, a nonzero probability of flow reversal exists because of the localized effects of the longitudinal vortices described earlier in moving fluid away from the surface.

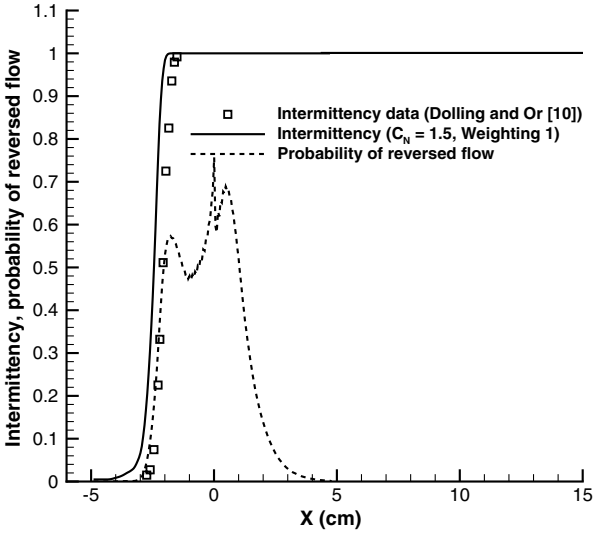

Fig. 12 Intermittency and probability of reversed-flow distributions.

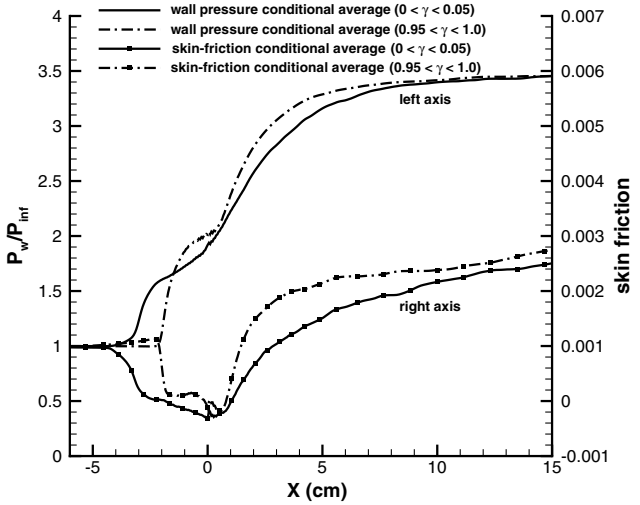

Fig. 13 Conditionally averaged surface-pressure and skin-friction distributions.

Figure 13 plots wall-pressure and skin-friction distributions conditionally averaged based on the intermittency distribution. Distributions associated with the most upstream positioning of the shock ($0 < \gamma < 0.05$) and the most downstream positioning of the separation shock ($0.95 < \gamma < 1$) are shown. A larger estimate of $L_{SM} = \sim 1\ \delta_0$ can be obtained as the difference between the most upstream and most downstream positions of the initial pressure rise. The conditionally averaged skin-friction distributions show that the region of reversed flow is largest for the most upstream position of the separation shock and smallest when the shock is at its most downstream position. Piponniau et al.'s [39] conditional analysis of the near-surface velocity field in an oblique-shock/turbulent boundary-layer interaction shows a similar trend: a larger separation region is associated with the upstream movement of the separation shock.

Shock motion leads to a significant increase in the surface-pressure fluctuation intensity, as shown in Fig. 14. Two peaks are observed: one associated with separation and the other with reattachment. Because the average surface pressures are smaller at the separation point, the fluctuation intensity is largest at this location. All model predictions are in relatively good agreement with the peak value of ~0.15, but all models locate the peak further upstream. The fluctuation intensity upstream of the separation-shock position is best predicted by the new model with $C_N = 1.5$ and is higher than experiment both upstream of the separation shock and within the separated region for the new model with $C_N = 1.2$. The predictions are somewhat sensitive to the ensemble-averaging method used in the turbulence closure. Weighing method 2 produces a smaller peak intensity value that is in more accord with the experimental data. A rapid attenuation of the fluctuation intensity takes place after reattachment, but the intensity level is still significantly higher than that in the incoming boundary layer.

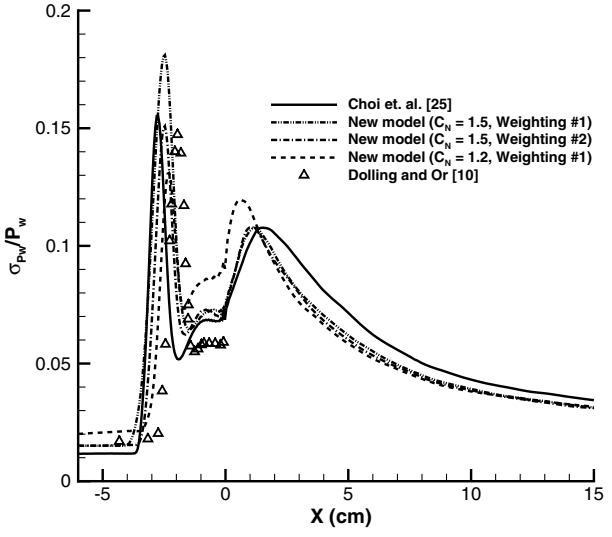

Fig. 14 Surface-pressure fluctuation intensity distributions.

Figure 15 presents probability density functions (PDFs) generated from the wall-pressure signal at different locations upstream, within, and downstream of the intermittent region. Nearly Gaussian distributions are maintained in the upstream boundary layer ($\gamma = 0$), within the separation region ($X = -0.66$ cm), and further downstream (not shown). Within the intermittent region, the signal is non-Gaussian, indicating the presence of localized events that force the wall pressure to be higher or lower than the mean. Good agreement with the data of Dolling and Or [10] is observed at all stations.

Figure 16 show snapshots of velocity magnitude extracted at locations just above the surface, at $Y/\delta_0 = 0.2$, and at $Y/\delta_0 = 0.7$. The contours are scaled to reveal small gradations in the velocity magnitude in the incoming boundary layer, with darker contours representing slower moving fluid. Near the wall, small streaklike structures in the incoming boundary layer interact with the nominally planar separation line. Excursions of low-momentum fluid onto the ramp surface indicated in the time-averaged skin-friction distributions (Fig. 6) are shown here in an instantaneous view. Broader, more elongated streaklike structures are found at $Y/\delta_0 = 0.2$. At $Y/\delta_0 = 0.7$, pockets of low- and high-momentum fluid are more uniformly dispersed and there is less organization overall, although some streaklike structures persist. The shock front (represented by the sharp gradation to darker contours) moves toward or away from the corner in response to the actions of higher-speed or lower-speed pockets of fluid. In some cases, the effects of a collection of such streaks with momentum lower or higher than the average causes the shock front to persist for a period of time at a location more upstream or downstream than the average, similar to the observations of Ganapathisubramani et al. [41]. In the data surveyed and in animations of the process, however, there is no clear indication of an upstream or downstream motion of the entire shock front. It appears that the intermittent responses mentioned above may be more due to

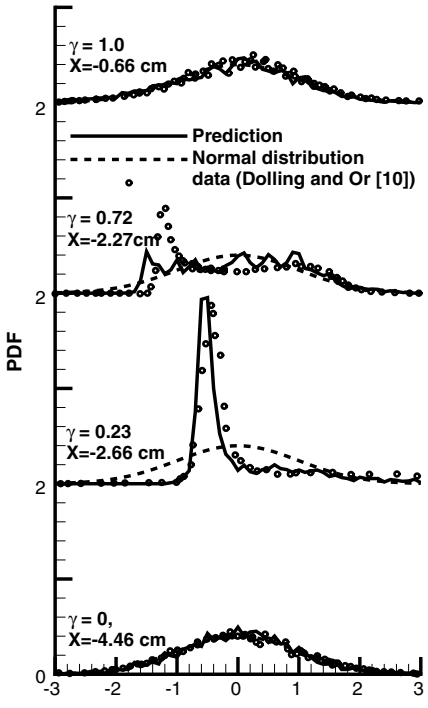

Fig. 15 PDFs of wall-pressure fluctuations upstream, within, and downstream of intermittent region.

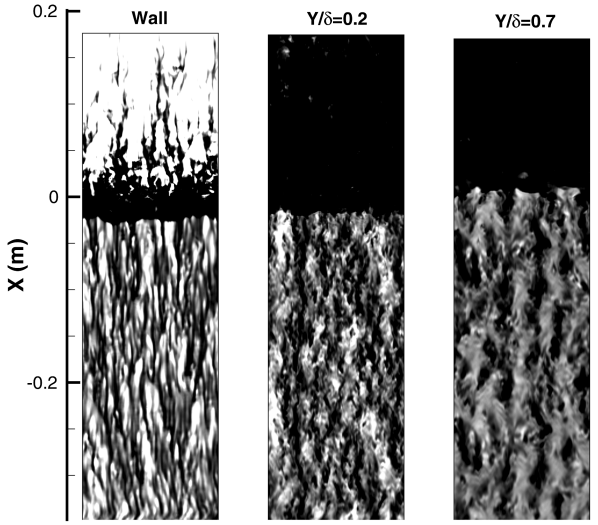

Fig. 16 Velocity magnitude snapshots extracted at different wall-normal planes.

these localized interactions than to a low-frequency motion of the entire shock front.

F. Spectral Analysis

Some low-frequency content can be observed in the power spectra, however, as shown in Fig. 17. Each power spectrum is normalized by the variance of the pressure signal and the frequency, as in [11,22,24], and a fast-Fourier transform technique, applied at different locations in the spanwise direction, is used to generate the spectra. Similar to Dupont et al. [11], four separate zones can be observed in the power spectrum corresponding to the wall pressure: 1) a typical turbulent boundary-layer spectrum characterized by broadband higher frequencies, located where $X < -0.04$; 2) a region around the shock location, $-0.03 < X < -0.017$, dominated by low frequencies; 3) a recovery zone, $-0.017 < X < 0$, where higher frequencies return to the spectrum although there are still significant midlevel frequencies; and 4) past the corner, $X > 0$, where the spectrum is once again dominated by higher frequencies typical to a turbulent boundary layer, although significant medium level frequencies remain far downstream of the interaction.

Dupont et al. [11] characterize their shock motion with a Strouhal number $S_L = f_{sh} L_{sep}/U_\infty$, where L_{sep} is the length of the separated region. The strongest interaction analyzed by Dupont et al. had a Strouhal number of 0.025. This value can be used to back out a shock-motion frequency corresponding to our conditions, shown in Fig. 17 as the white line. This frequency correlates well with the observed low-frequency peak in the shock-motion region. However, the power spectrum was obtained from data extracted over a relatively short time, ~0.01 s, so that the low-frequency part of the spectrum may not be statistically converged. It is also possible that a dominant lower frequency exists that could not be captured in the time interval considered and that the true peak is not at the observed frequency.

Figure 17 also shows power spectra at $Y/\delta_0 = 0.7$. Here, the spectrum is more scattered and smeared compared to that at the wall. This is probably due to turbulent/nonturbulent interactions (see Fig. 1 for the location of this plane). There are several high-frequency bands that persist unaltered throughout the interaction. These likely are due to the recycling technique used to sustain the turbulence at the inflow. A trace of the recycling-plane frequency ($U_\infty/(8\delta_0)$) can be seen in the spectrum, as can harmonics of this frequency.

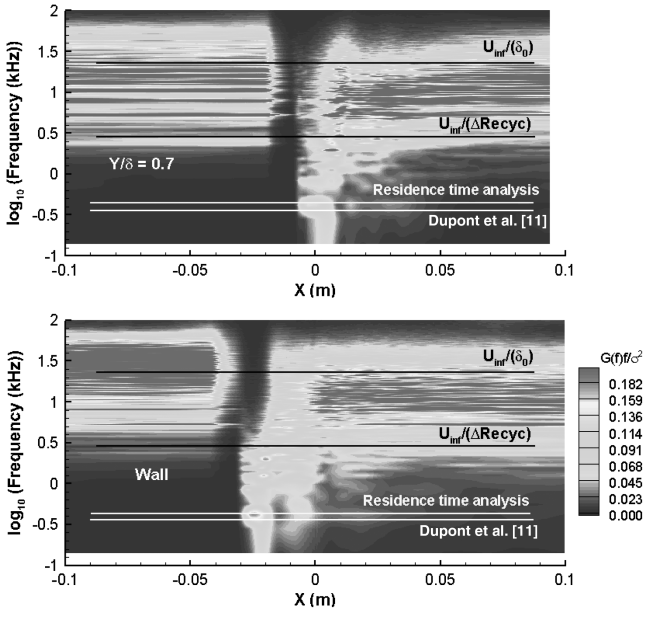

Fig. 17 Spectral maps extracted at different Y locations.

G. Residence Time Distributions

The fact that a large amount of experimental data can be collapsed into a relatively narrow range of Strouhal numbers according to the above expression [11] suggests that the dominant time scale may be one associated with entrainment of fluid into and out of the recirculation region, which naturally would scale with the length of the separation region. To explore this, a collection of 4000 evenly distributed streamlines passing through the separation region were analyzed to determine the amount of time that fluid particles would spend in this region. A time-mean solution was used in this analysis. To estimate a characteristic time for each streamline, a line integral of the reciprocal of the velocity magnitude was performed along the path of each streamline, starting when the streamline crossed $X = -0.025$ m and ending once it had crossed $X = 0.015$ m. Streamlines that began or ended within these bounds were discarded, as these were not considered representative of net fluid entrainment into the recirculation region. Figure 18 shows a top view of an ensemble of near-surface streamlines for the 20 deg interaction. As shown earlier in Fig. 6, a weakly separated flow, characterized by significant spanwise migration of fluid particles and complex topological features, is found in the region of intermittent separation-shock motion.

Based on the times calculated for each streamline, a PDF for the residence time distribution can be created, as shown in Fig. 19. The average residence time for streamlines located within the gray rectangle of Fig. 19 (the more probable values) is 2.3e − 3 s. The associated frequency is 0.434 kHz, which is indicated as a line in Fig. 17. This value is close to the shock-motion frequency predicted

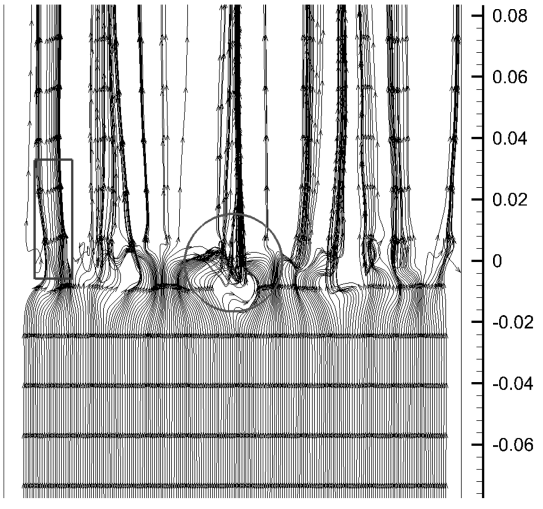

Fig. 18 Streamlines entering separation region (view from above).

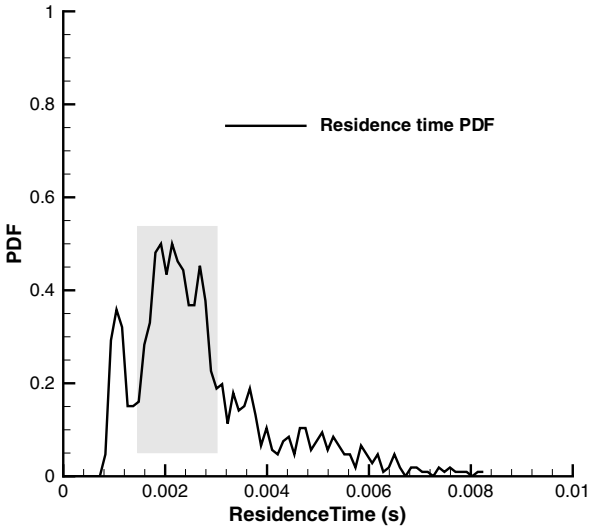

Fig. 19 Residence time distribution.

for this case by the Dupont et al. [11] correlation and nearly coincides with the dominant low-frequency signal in the spectral map. These results show a connection between the observed low-frequency signal and the most probable time required for fluid to enter and leave the recirculation zone. More recent experimental results [11,39] and computational predictions [20,22,38,42] indicate that the origin of the low-frequency component is likely related to the dynamics and structure of the separation zone itself rather than to the characteristics of the incoming boundary layer. This new result provides additional evidence to support this general argument. The fact that residence time distributions of this type can be obtained from three-dimensional mean-flow data suggests that it may be possible to predict a dominant low-frequency mode without conducting an unsteady analysis. Recent results for a 24 deg compression-ramp interaction [43] also show a strong correlation between the dominant low-frequency signal and the most probable residence time, but further study will be required to determine whether this observation extends to other shock/boundary-layer interactions. A more accurate residence time distribution might be obtained by sampling fluid path lines from an ensemble of instantaneous snapshots: this again will be a subject for future work.

V. Conclusions

Two large-eddy simulation (LES)/Reynolds-averaged Navier–Stokes (RANS) models have been applied to a shock/boundary interaction generated by a 20 deg compression corner. The models are designed to transition from unsteady RANS to LES as the boundary layer shifts from its logarithmic behavior to its wakelike response, but they differ in that the earlier model requires the preselection of a model constant for each case, while the newer model avoids this difficulty. Predictions are compared with mean-flow and second-moment experimental data obtained at Princeton University. In general, calculated mean-flow velocity, surface-pressure, and surface skin-friction distributions agree well with the experiment, with the most noticeable discrepancy being a slight overprediction of the level of upstream influence induced by the shock wave. The newer LES/RANS model provides improved predictions of mean-flow properties. Comparisons with mass-flux fluctuation intensity, Reynolds axial stress, and Reynolds shear-stress profiles have also been presented. The LES/RANS models accurately capture the amplification of the Reynolds axial stress, but the results exhibit some deviations from experiment just downstream of the separation region, where the mean-flow response is not particularly well predicted. The models overpredict the experimental Reynolds shear-stress levels in the recovery region. The LES/RANS results have also been used to study aspects of separation-shock unsteadiness. Calculated shock-position intermittency distributions, wall-pressure probability density functions, and wall-pressure fluctuation intensity distributions are in good agreement with experimental data. Wall-pressure power spectra show a distinct shift to a dominant low-frequency component centered about the time-averaged position of the separation shock and extending into the backflow region. The dominant low-frequency wall-pressure signal is well correlated with a frequency associated with the most probable residence time of fluid within the recirculation region. The measurable effects of separation-shock intermittency also appear to be influenced by the passage of coherent, streaklike structures through the shock front.

Acknowledgments

This work is supported by U.S. Army Research Office grant W911NF-08-1-0430, monitored by Frederick Ferguson. The authors gratefully acknowledge Rodney Bowersox of Texas A&M University for providing information relating to hot-wire anemometry and the use of the strong Reynolds analogy.

References

[1] Adamson, T. C., and Messiter, A. F., "Analysis of Two-Dimensional Interactions Between Shock Waves and Boundary Layers," *Annual Review of Fluid Mechanics*, Vol. 12, 1980, pp. 103–138. doi:10.1146/annurev.fl.12.010180.000535

[2] Fernholz, H. H., Finley, P. J., Dussuage, J. P., and Smits, A. J., "A Survey of Measurements and Measuring Techniques in Rapidly Distorted Compressible Turbulent Boundary Layers," AGARDograph 315, 1989.

[3] Delery, J., and Panaras, A., "Shock-Wave/Boundary Layer Interactions in High Mach Number Flows," AGARD AR-319, Vol. 1, May 1996.

[4] Settles, G. S., Fitzpatrick, T. J., and Bogdanoff, S. M., "Detailed Study of Attached and Separated Compression Corner Flowfields in High Reynolds Number Supersonic Flow," *AIAA Journal*, Vol. 17, 1979, pp. 579–585. doi:10.2514/3.61180

[5] Smits, A. J., and Muck, K.-C., "Experimental Study of Three Shock Wave/Turbulent Boundary Layer Interactions," *Journal of Fluid Mechanics*, Vol. 182, 1987, pp. 291–314. doi:10.1017/S0022112087002349

[6] Settles, G. S., and Dodson, L. J., "Supersonic and Hypersonic Shock/Boundary Layer Interaction Database," *AIAA Journal*, Vol. 32, No. 7, 1994, pp. 1377–1383. doi:10.2514/3.12205; also NASA CR 177577, 1991.

[7] Settles, G. S., and Dodson, L. J., "Hypersonic Shock/Boundary-Layer Interaction Database: New and Corrected Data," NASA CR 177638, 1994.

[8] Donovan, J. F., Spina, E. F., and Smits, A. J., "The Structure of a Supersonic Turbulent Boundary Layer Subjected to Concave Surface Curvature," *Journal of Fluid Mechanics*, Vol. 259, 1994, pp. 1–24. doi:10.1017/S0022112094000017

[9] Dolling, D. S., and Murphy, M. T., "Unsteadiness of the Separation Shock Wave Structure in a Supersonic Compression Ramp Flowfield," *AIAA Journal*, Vol. 21, 1983, pp. 1628–1634. doi:10.2514/3.60163

[10] Dolling. D. S., and Or, C. T., "Unsteadiness of the Shock Wave Structure in Attached and Separated Compression Ramp Flows," *Experiments in Fluids*, Vol. 3, 1985, pp. 24–32. doi:10.1007/BF00285267

[11] Dupont, P., Haddad, C., and Debieve, J. F., "Space and Time Organization in a Shock-Induced Separated Boundary Layer," *Journal of Fluid Mechanics*, Vol. 559, 2006, pp. 255–277. doi:10.1017/S0022112006000267

[12] Panaras, A., "The Effect of the Structure of Swept-Shock Wave/Turbulent Boundary Layer Interactions on Turbulence Modelling," *Journal of Fluid Mechanics*, Vol. 338, 1997, pp. 203–230. doi:10.1017/S0022112097004825

[13] Edwards, J. R., and Chandra, S., "Eddy Viscosity—Transport Turbulence Models for High-Speed, Two-Dimensional, Shock-Separated Flowfields," AIAA Paper 1994-0310, Jan. 1994.

[14] Liou, W. W., Huang, G., and Shih, T. H., "Turbulence Model Assessment for Shock-Wave/Turbulent Boundary Layer Interaction in Transonic and Supersonic Flows," *Computers and Fluids*, Vol. 29, 2000, pp. 275–299. doi:10.1016/S0045-7930(99)00010-9

[15] Rizzetta, D. P., "Evaluation of Explicit Algebraic Reynolds-Stress Models for Separated Supersonic Flows," *AIAA Journal*, Vol. 36, No. 1, 1998, pp. 24–30.

doi:10.2514/2.370
[16] Gerolymos, G. A., Sauret, E., and Vallet, I., "Oblique-Shock-Wave/Boundary Layer Interaction Using Near-Wall Reynolds-Stress Models," *AIAA Journal*, Vol. 42, No. 6, 2004, pp. 1089–1100. doi:10.2514/1.1984
[17] Knight, D., and Degrez, G., "Shock Wave/Boundary Layer Interactions in High Mach Number Flows: A Critical Survey of Current CFD Prediction Capabilities," AGARD AR-319, Vol. 2, 1997.
[18] Wu, M., and Martin, M. P., "Direct Numerical Simulation of Supersonic Turbulent Boundary Layer over a Compression Ramp," *AIAA Journal*, Vol. 45, No. 4, 2007, pp. 879–889. doi:10.2514/1.27021
[19] Wu, M., and Martin, M. P., "Analysis of Shock Motion in Shockwave and Turbulent Boundary Layer Interaction Using Direct Numerical Simulation Data," *Journal of Fluid Mechanics*, Vol. 594, 2008, pp. 71–83. doi:10.1017/S0022112007009044
[20] Pirozzoli, S., and Grasso, F., "Direct Numerical Simulation of Impinging Shock Wave/Turbulent Boundary Layer Interaction at $M = 2.25$,"*Physics of Fluids*, Vol. 18, No. 6, 2006, Paper 065113. doi:10.1063/1.2216989
[21] Garnier, E., Sagaut, P., and Deville, M., "Large Eddy Simulation of Shock/Boundary Layer Interaction," *AIAA Journal*, Vol. 40, 2002, p. 1935. doi:10.2514/2.1552
[22] Touber, E., and Sandham, N. D., "Large-Eddy Simulation of Low-Frequency Unsteadiness in a Turbulent Shock-Induced Separation Bubble," *Theoretical and Computational Fluid Dynamics*, Vol. 23, 2009, pp. 79–107. doi:10.1007/s00162-009-0103-z
[23] Loginov, M. S., Adams, N. A., and Zheltovodov, A. A., "Large Eddy Simulation of Shock-Wave/Turbulent-Boundary-Layer Interaction," *Journal of Fluid Mechanics*, Vol. 565, 2006, pp. 135–169. doi:10.1017/S0022112006000930
[24] Edwards, J. R., Choi, J.-I., and Boles, J. A., "Hybrid Large-Eddy/Reynolds-Averaged Navier–Stokes Simulation of a Mach-5 Compression Corner Interaction," *AIAA Journal*, Vol. 46, No. 4, 2008, pp. 977–991. doi:10.2514/1.32240
[25] Choi, J.-I., Edwards, J. R., and Baurle, R. A., "Compressible Boundary Layer Predictions at High Reynolds Number Using LES/RANS Models," *AIAA Journal*, Vol. 47, No. 9, 2009, pp. 2179–2193. doi:10.2514/1.41598
[26] Gieseking, D. A., Choi, J.-I., Edwards, J. R., and Hassan, H. A., "Compressible Flow Simulations Using a New LES/RANS Model," *AIAA Journal*, Vol. 49, No. 10, 2011, pp. 2194–2209. doi:10.2514/1.J051001
[27] Garnier, E., "Stimulated Detached Eddy Simulation of Three-Dimensional Shock/Boundary Layer Interaction," *Shock Waves*, Vol 19, 2009, pp. 479–486. doi:10.1007/s00193-009-0233-7
[28] Shur, M., Spalart, P. R., Strelets, M., and Travin, A. K., "A Hybrid RANS/LES Approach with Delayed DES and Wall-Modeled LES Capabilities," *International Journal of Heat and Fluid Flow*, Vol. 29, 2008, pp. 1638–1649. doi:10.1016/j.ijheatfluidflow.2008.07.001
[29] Menter, F. R., "Two-Equation Eddy-Viscosity Turbulence Models for Engineering Applications," *AIAA Journal*, Vol. 32, No. 8, Aug. 1994, pp. 1598–1605. doi:10.2514/3.12149
[30] Lenormand, E., Sagaut, P., Ta Phuoc, L., and Comte, P., "Subgrid-Scale Models for Large-Eddy Simulations of Compressible, Wall-Bounded Flows," *AIAA Journal*, Vol. 38, 2000, pp. 1340–1350. doi:10.2514/2.1133
[31] Boles, J. A., Choi, J.-I., Edwards, J. R., and Baurle, R. A., "Simulations of High-Speed Internal Flows Using LES/RANS Models" AIAA Paper 2009-1324, 2009.
[32] Colella, P., and Woodward, P. R., "The Piecewise Parabolic Method (PPM) for Gas-Dynamical Simulations," *Journal of Computational Physics*, Vol. 54, pp. 174–201. doi:10.1016/0021-9991(84)90143-8, 1984.
[33] Ducros, F., Ferrand, V., Nicaud, F., Weber, C., Darracq, D., Gachareiu, C., and Poinsot, T., "Large-Eddy Simulation of the Shock/Turbulence Interaction," *Journal of Computational Physics*, Vol. 152, No. 2, 1999, pp. 517–549. doi:10.1006/jcph.1999.6238
[34] Morkovin, M. V., "Effects of Compressibility on Turbulent Flows," *Mecanique de la Turbulence*, edited by A. Favre, Centre National de la Recherche Scientifique, Paris, 1962, pp. 367–380.
[35] Kistler, A. L., "Fluctuation Measurements in a Supersonic Turbulent Boundary Layer," *Physics of Fluids*, Vol. 2, No. 3, 1959, pp. 290–296. doi:10.1063/1.1705925
[36] Dussauge, J. P., and Gaviglio, J., "Bulk Dilatation Effects on Reynolds Stress in the Rapid Expansion of a Turbulent Boundary Layer at Supersonic Speed," *Proceedings of the 3rd Symposium on Turbulent Shear Flows*, Davis, CA, Vol. 2, Springer–Verlag, Berlin, 1981, pp. 33–38.
[37] Kuntz, D. W., Amatucci, V. A., and Addy, A. L., "Turbulent Boundary Layer Properties Downstream of the Shock-Wave/Boundary Layer Interaction," *AIAA Journal*, Vol. 25, No. 5, 1987, pp. 668–675. doi:10.2514/3.9681
[38] Priebe, S., and Martin, M. P., "Low-Frequency Unsteadiness in DNS of Shock Wave/Turbulent Boundary Layer Interaction," AIAA Paper 2011-0725, Jan. 2011.)
[39] Piponniau, S., Dussauge, J. P., Debieve, J. F., and Dupont, P., "A Simple Model for Low Frequency Unsteadiness in Shock-Induced Separation," *Journal of Fluid Mechanics*, Vol. 629, 2009, pp. 87–108. doi:10.1017/S0022112009006417
[40] Debieve, J. F., Gouin, H., and Gaviglio, J., "Evolution of the Reynolds Stress Tensor in a Shock/Turbulence Interaction," *Indian Journal of Technology*, Vol. 20, 1982, pp. 90–97.
[41] Ganapathisubramani, B., Clemens, N. T., and Dolling, D. S., "Effects of Upstream Boundary Layer on the Unsteadiness of Shock-Induced Separation," *Journal of Fluid Mechanics*, Vol. 585, 2007, pp. 369–394. doi:10.1017/S0022112007006799
[42] Touber, E., and Sandham, N. D., "Low-Order Stochastic Modeling of Low-Frequency Motions in Reflected Shock-Wave/Boundary Layer Interactions," *Journal of Fluid Mechanics*, Vol. 671, 2011, pp. 417–465. doi:10.1017/S0022112010005811
[43] Gieseking, D. A., Edwards, J. R., and Choi, J.-I., "Simulation of a Mach 3 24 Degree Compression-Ramp Interaction Using LES/RANS Models," AIAA Paper 2011-5541, Aug. 2011.

G. Blaisdell
Associate Editor